

# Deep Bottom Mixed Layer Drives Intrinsic Variability of the Antarctic Slope Front

WILMA GERTRUD CHARLOTTE HUNEKE

*Institute for Marine and Antarctic Studies, and ARC Centre of Excellence for Climate System Science,  
University of Tasmania, Hobart, Tasmania, Australia*

ANDREAS KLOCKER

*Antarctic Climate and Ecosystems Cooperative Research Centre, and ARC Centre of Excellence for Climate Extremes,  
University of Tasmania, Hobart, Tasmania, Australia*

BENJAMIN KEITH GALTON-FENZI

*Australian Antarctic Division, Kingston, and Antarctic Climate and Ecosystems Cooperative Research Centre,  
University of Tasmania, Hobart, Tasmania, Australia*

(Manuscript received 27 February 2019, in final form 20 September 2019)

## ABSTRACT


The Antarctic Slope Front (ASF) is located along much of the Antarctic continental shelf break and helps to maintain a barrier to the movement of Circumpolar Deep Water (CDW) onto the continental shelf. The stability of the ASF has a major control on cross-shelf heat transport and ocean-driven basal melting of Antarctic ice shelves. Here, the ASF dynamics are investigated for continental shelves with weak dense shelf water (DSW) formation, which are thought to have a stable ASF, common for regions in East Antarctica. Using an ocean process model, this study demonstrates how offshore bottom Ekman transport of shelf waters leads to the development of a deep bottom mixed layer at the lower continental slope, and subsequently determines an intrinsic variability of the ASF. The ASF variability is characterized by instability events that affect the entire water column and occur every 5–10 years and last for approximately half a year. During these instability events, the cross-shelf density gradient weakens and CDW moves closer to the continent. Stronger winds increase the formation rate of the bottom mixed layer, which causes a subsequent increase of instability events. If the observed freshening trend of continental shelf waters leads to weaker DSW formation, more regions might be vulnerable for the ASF variability to develop in the future.

## 1. Introduction

The Antarctic Slope Front (ASF) and the associated Antarctic Slope Current (ASC) are thought to be almost circumpolar (see [appendix D](#) for a complete list of the acronyms used in this paper). The ASF is a manifestation of the barrier to cross-slope flow posed by the topographic potential vorticity (PV) gradient and is important in regulating movement of Circumpolar Deep Water (CDW) onto the Antarctic continental shelf ([Jacobs 1991](#); [Whitworth et al. 1998](#); [Thompson et al. 2018](#)).

CDW is a relatively warm and salty water mass that is typically found in the Antarctic Circumpolar Current (ACC), but once it crosses the continental shelf break and enters ice shelf cavities, usually as a modified version, it has the potential to drive strong basal melting and to influence the stability of the Antarctic ice sheet (e.g., see reviews by [Dinniman et al. 2016](#); [Silvano et al. 2016](#)).

A stable ASF can isolate the colder continental shelf waters from the warmer CDW offshore ([Jacobs 1991](#)). Warm continental shelf temperatures and high basal melt rates are consequently observed in the Amundsen and Bellingshausen Seas, where the ASF is absent or very weak due to the local atmospheric circulation pattern and the close proximity of the ACC to the shelf break ([Pritchard et al. 2012](#); [Petty et al. 2013](#); [Rignot et al. 2013](#)). Elevated melt rates also occur in regions

 Denotes content that is immediately available upon publication as open access.

*Corresponding author:* Wilma Gertrud Charlotte Huneke, [wilma.huneke@utas.edu.au](mailto:wilma.huneke@utas.edu.au)

DOI: 10.1175/JPO-D-19-0044.1

© 2019 American Meteorological Society. For information regarding reuse of this content and general copyright information, consult the [AMS Copyright Policy](#) ([www.ametsoc.org/PUBSReuseLicenses](http://www.ametsoc.org/PUBSReuseLicenses)).

characterized by submarine troughs, which connect the open ocean with ice shelf cavities, and effectively channel the warm CDW onto the continental shelf [e.g., near the Totten Glacier in East Antarctica (Rintoul et al. 2016; Nitsche et al. 2017) or the Marguerite Trough in West Antarctica (Moffat et al. 2009; St-Laurent et al. 2013)]. In the absence of troughs, the export of dense shelf water (DSW) can trigger mesoscale instabilities that weaken the ASF (Stewart and Thompson 2016). Pulses of intruding warm water related to eddy activity have been modeled using high resolution process models (e.g., Stewart and Thompson 2015) and observed in the northwestern Weddell Sea (Thompson et al. 2014).

Little is known about processes that may destabilize the ASF at sections around the Antarctic coastline with weak DSW production and no major troughs [e.g., along sections in East Antarctica (Thompson et al. 2018)]. This study assesses the physics relevant for the Antarctic continental shelf and slope under such conditions in an ocean process model. The results show that downslope bottom Ekman transport of relatively fresh and therefore buoyant continental shelf water may lead to a deep bottom mixed layer at the lower Antarctic continental slope. The continuous freshwater input from the continental shelf region leads to bottom mixed layer instabilities that drive an intrinsic variability of the ASF. During the ASF instability events, the cross-slope density gradient relaxes and relatively warm CDW moves closer to the continental shelf break.

## 2. Process model of the continental shelf break ocean system

The numerical ocean model used in this study is the open source community Regional Ocean Modeling System (ROMS) version 3.6, a hydrostatic three-dimensional primitive equation finite difference model (Shchepetkin and McWilliams 2005), which is run using a nonlinear equation of state (see appendix A for more information). The version of ROMS used here includes ice shelves and has previously been used to simulate high southern latitudes (e.g., Dinniman et al. 2011, 2012; Galton-Fenzi et al. 2012; Cougnon et al. 2013; Gwyther et al. 2014). The Coriolis parameter varies linearly on a  $\beta$ -plane locating the study area at about 64°–68°S (appendix A). The model domain is 400 km (along-slope/zonal direction)  $\times$  550 km (cross-slope/meridional direction)  $\times$  3 km (depth) and is a reentrant channel in the along-slope direction with a symmetric geometry (Fig. 1). The total depth  $h(j)$  for each grid cell  $j$  in cross-slope direction is a function of the cross-slope distance  $y(j)$  and follows

$$h(j) = H_s + \frac{H - H_s}{2} \left\{ 1 + \frac{2\pi \tanh[y(j) - L_{slc}]}{L_{sl}} \right\} \quad (1)$$

with the continental shelf depth  $H_s$ , the maximum depth  $H$ , the center of the slope  $L_{slc}$  and the slope width  $L_{sl}$ . The mean slope is 1.6%, which is similar to slopes found along 110°–125°E in East Antarctica. The southernmost 100 km of the domain are covered by an ice shelf with depth  $z_{ice}(j)$ , given as

$$z_{ice}(j) = \begin{cases} -H_{ic} + \arctan \left[ \frac{y(j)\pi}{2(L_{ic} - L_{icf})} \right] (H_{ic} - H_{icf}), & \text{for } 0 \leq y(j) \leq L_{ic} - L_{icf}, \\ -H_{icf} + \frac{y(j) - (L_{ic} - L_{icf})}{L_{icf}} H_{icf}, & \text{for } L_{ic} - L_{icf} \leq y(j) \leq L_{ic}, \\ 0, & \text{for } L_{ic} \leq y(j), \end{cases} \quad (2)$$

with the maximum ice shelf depth  $H_{ic}$ , the depth at the front  $H_{icf}$  and the respective cross-slope distances  $L_{ic}$  and  $L_{icf}$ . The ice shelf base is coupled thermodynamically to the ocean following Galton-Fenzi et al. (2012). The ice-shelf thermodynamics account for the effect of basal melting and related changes in water mass properties and dynamics. The cold ice shelf cavity temperature induces a melt rate of approximately  $0.03 \text{ m yr}^{-1}$  which is small compared to observed melt rates of, for example,  $0.6 \text{ m yr}^{-1}$  at the Amery ice shelf (Galton-Fenzi et al. 2012; Depoorter et al. 2013; Rignot et al. 2013), see also

appendix B. The salinity on the continental shelf is approximately 0.01 psu higher in a model run without thermodynamics under the ice shelves. Hence, the water mass composition on the continental shelf is predominantly set by the surface restoring.

The model grid has a horizontal resolution of 1 km and 30 vertical layers that are equally intensified near the surface and bottom using terrain-following vertical coordinates (Fig. 1b). The average vertical cell thickness in the ocean interior is 34 m on the continental shelf, 121 m at the continental slope, and 205 m in the

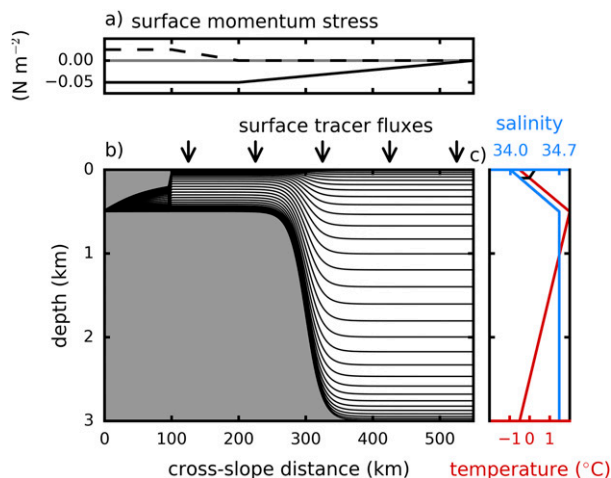


FIG. 1. Setup of zonally symmetric process model. (a) Along-slope (solid) and cross-slope (dashed) surface momentum stress. (b) Bathymetry, ice shelf draft, and terrain-following vertical layers (30 levels) on a cross-slope section. (c) Temperature (red) and salinity (blue) profiles prescribed at the northern boundary. The same profiles are applied to the entire domain as initial conditions with a minor adaptation to the salinity profile in the upper 100 m (black). The salinity increases at the surface to create an unstable stratification, which allows instabilities to develop in the zonally symmetric domain.

deep ocean. The thickness of the surface and bottom grid cells varies between 4, 11, and 20 m, respectively. To justify the choice of grid resolution a resolution analysis has been performed (see [appendix B](#)) with the aim to resolve mesoscale dynamics which have been identified to substantially control cross-shelf heat exchange ([Dinniman et al. 2016](#)).

The model configuration uses a fourth-order centered advection scheme, the *K*-profile parameterization (KPP) mixing scheme ([Large et al. 1994](#)) that accounts for convective mixing due to shear instability, double-diffusive mixing, and the vertical mixing of momentum and tracer in the mixed layer, and uses a quadratic bottom stress of  $3 \times 10^{-3}$ . A complete list of the specific parameter choices is given in [Tables A1](#) and [A2](#), and the applied C-preprocessor (CPP) options are given in [Tables A3](#) and [A4](#) in [appendix A](#).

The western and eastern boundaries are periodic while the northern boundary is clamped to salinity and temperature profiles that are representative of the Southern Ocean ([Fig. 1c](#)) and are the source of CDW in the domain. The initial conditions use the same values as the northern boundary profiles. However, in order to develop eddies in the zonally symmetric domain, the stratification of the upper water column has been made statically unstable in the entire domain by changing the salinity profile in the upper 100 m ([Fig. 1c](#), black line).

Additionally, three randomly distributed grid cells of the otherwise zero momentum field were initialized with a small zonal and meridional velocity of  $10^{-5} \text{ m s}^{-1}$ . Without these changes, the flow field does not become unstable. The model is initially spun up for 25 years to equilibrate water masses over the continental shelf region, which can be monitored by the basal melt rate of the ice shelf. The model is then restarted and run for 30 years before it is integrated for an additional 22 years (year 30–51) with output every three months and for another 6 years (year 52–57) with daily output to allow an analysis at higher temporal resolution. The geometric symmetry in along-slope direction allows the calculation of zonal means, which has been done for all diagnostics presented.

The applied surface forcing ensures that only weak DSW forms on the continental shelf. The surface grid cells are relaxed to a temperature of  $-1.85^{\circ}\text{C}$  and a salinity of 34.45 psu, modulated by a relaxation time scale of 60 days (see [appendix C](#) for a detailed description). The main component of the surface momentum stress is oriented in an along-slope direction (westward) with a smaller cross-slope component representing the northward katabatic wind ([Fig. 1a](#)). The applied momentum stress profile is based on the COREv2 climatology ([Large and Yeager 2009](#)) at sections along  $110^{\circ}$ – $125^{\circ}\text{E}$  in East Antarctica. This region is characterized by ice shelves along the margin, and no or only weak DSW production. Two additional sensitivity experiments are performed with 50% and 150% momentum stress of the control run. All simulations represent constant winter conditions.

### 3. Results

#### a. Simulated structure of the ASF and ASC

At the continental shelf break, the isopycnals slope down to the seabed in an onshore direction, as there is neither dense bottom water actively formed nor prescribed at the lateral boundaries which would force the isopycnals to lift and flatten, or even reverse ([Fig. 2a](#)). An ASC is produced with a dominant along-slope westward component with maximum values of around  $0.3 \text{ m s}^{-1}$  near the surface in the ASF region ([Fig. 2a](#)). The maximum of the ASC is located 25 km offshore from the center of the bathymetric slope. In the presence of a cross-shelf density gradient and in agreement with the thermal wind balance, the velocity decreases toward the bottom. The simulated ASC speed compares well with both observations ([Bindoff et al. 2000](#)) and realistic modeling work that has been done in East Antarctica ([Mathiot et al. 2011](#); [Gwyther et al. 2014](#)). On the

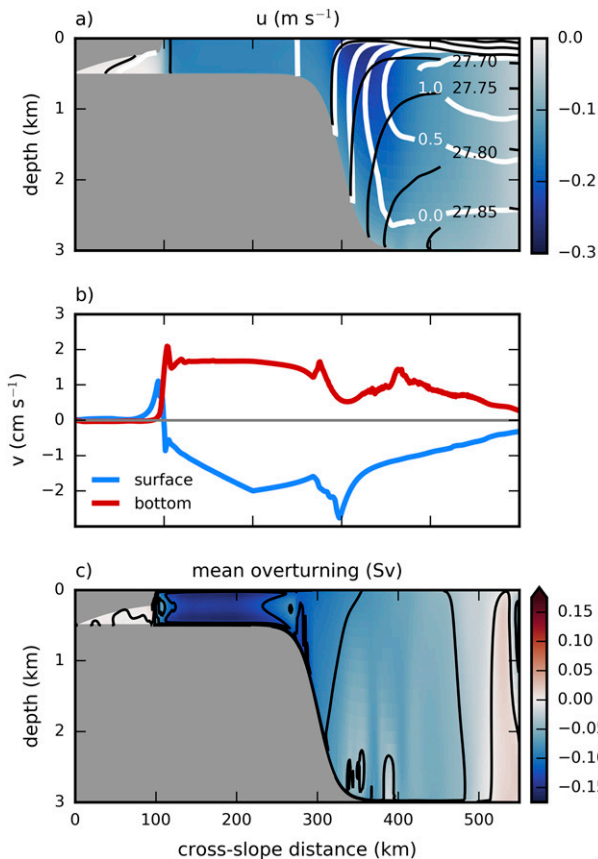


FIG. 2. (a) Cross-slope section showing zonal mean along-slope velocities at the beginning of year 55. Density contours are black, and temperature contours are white. (b) Associated surface (blue) and bottom (red) cross-slope velocity. Negative velocities are to the south (onshore) and positive velocities are to the north (offshore). (c) Mean overturning streamfunction with a contour interval of 0.1 Sv, see text for the calculation. Negative values (blue) indicate an anticyclonic (anticlockwise) circulation.

continental shelf, stratification is weak and the along-slope velocities are approximately  $0.1 \text{ m s}^{-1}$  in a westward direction.

The cross-slope velocity field on the continental shelf is an order of magnitude weaker than the along-slope velocity and consists of an onshore surface Ekman transport and an offshore bottom Ekman return flow (Figs. 2b,c). The cross-slope circulation on the continental shelf is confined to the top and bottom 100 m, respectively, as indicated by the mean overturning stream in Fig. 2c. The streamfunction,

$$\Psi = L_x \int_z^0 \bar{v} dz, \quad (3)$$

is calculated as the vertical integral of the along-slope average (overbar) of the cross-slope velocity  $v$

(positive to the north) multiplied by the domain width  $L_x$  in order to obtain an overturning transport ( $1 \text{ Sv} \equiv 10^6 \text{ m}^3 \text{ s}^{-1}$ ).

### b. Instability of the ASF

The main part of the ASF is located in a region 300–340 km from the southern boundary and extends throughout the water column (Figs. 3c,d between blue and green line). Figure 3a shows the ocean heat content HC for this region, which is given by

$$\text{HC} = \sum_{i,j,k} T_{i,j,k} \rho_{i,j,k} c_p \Delta V_{i,j,k}, \quad (4)$$

where  $T$  (measured in kelvins) is the ocean temperature,  $c_p = 3974 \text{ J kg}^{-1} \text{ K}^{-1}$  is the specific heat capacity of polar ocean seawater,  $\rho$  is the in situ density, and  $\Delta V$  is the volume of each cell ( $i, j, k$ ), where  $i$  is the cross-slope index and  $k$  the vertical index. Similar, Fig. 3b shows the ocean heat transport (HT), which is given by

$$\text{HT} = \sum_{i,k} v_{i,k} T_{i,k} \rho_{i,k} c_p \Delta A_{i,k}, \quad (5)$$

where  $\Delta A$  is the area of a cell, across an along-slope section at 300 and 340 km north of the southern boundary.

The HC time series reveals that the ASF contains an intrinsic variability (Fig. 3a). During the 27-yr length of output shown, four instability events occur with an aperiodic timing of approximately 5–10 years. The instability events are of varying intensities and each event lasts approximately 6–9 months. Between two instability events, the HC has a negative trend and the ASF strengthens: the isopycnals steepen and move offshore (see isopycnals in Figs. 3c,d as well as in Fig. 5). As a consequence, the heat is also moving offshore which is indicated by the positive sign of the HT (Fig. 3b). During an instability event phase, the southward transport of heat toward the ASF region increases (green line in Fig. 3b) while the transport onto the continental shelf itself is almost constant (blue line in Fig. 3b), and the HC consequently also increases.

Cross sections of temperature and density just before (year 48, Fig. 3c) and during (year 49, Fig. 3d) an instability event show the change in the density field which enables CDW to move across-slope. The associated surface temperature distributions are shown in Figs. 3e and 3f. The net heat transport across the continental slope averaged over the four events shown in Figs. 3a and 3b is  $2 \times 10^{11} \text{ J s}^{-1}$  in an offshore direction as surface waters (flowing onshore) are colder than the deep waters (flowing offshore). The exact value will

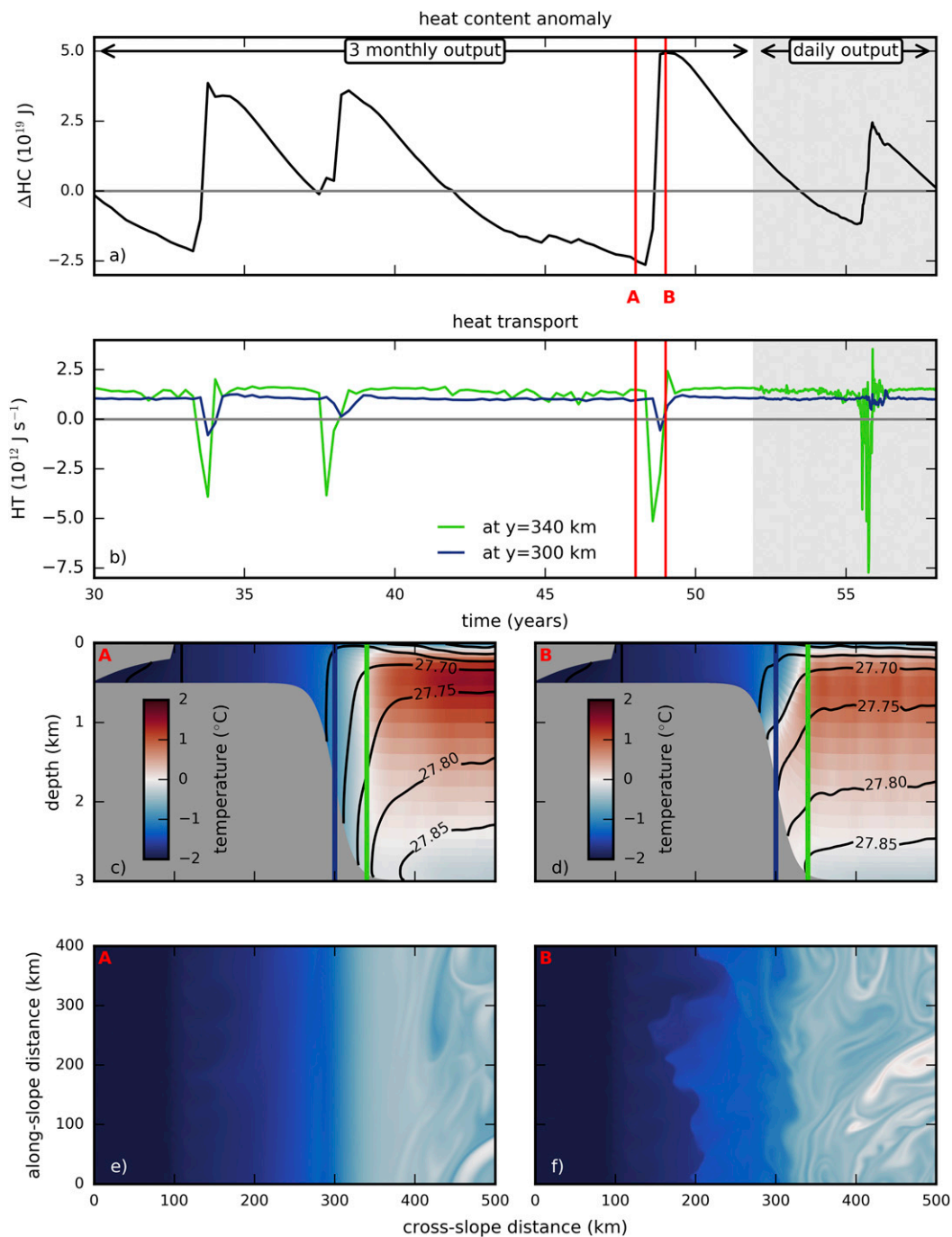


FIG. 3. (a) Time series of change (anomaly with respect to year 30) in ocean heat content for the region 300–340 km from the southern boundary as indicated by the blue and green vertical line in (c) and (d). (b) Time series of ocean heat transport through the boundaries. The gray horizontal line is the zero value, and gray shading indicates a time frame with higher (daily) output that is shown in Fig. 4. (c),(d) Zonal mean temperature with density contours at year 48 [red vertical line labeled A in (a)] and at year 49 [red vertical line labeled B in (a)]. (e),(f) Associated surface temperature distribution, with the colorbar as in (c) and (d).

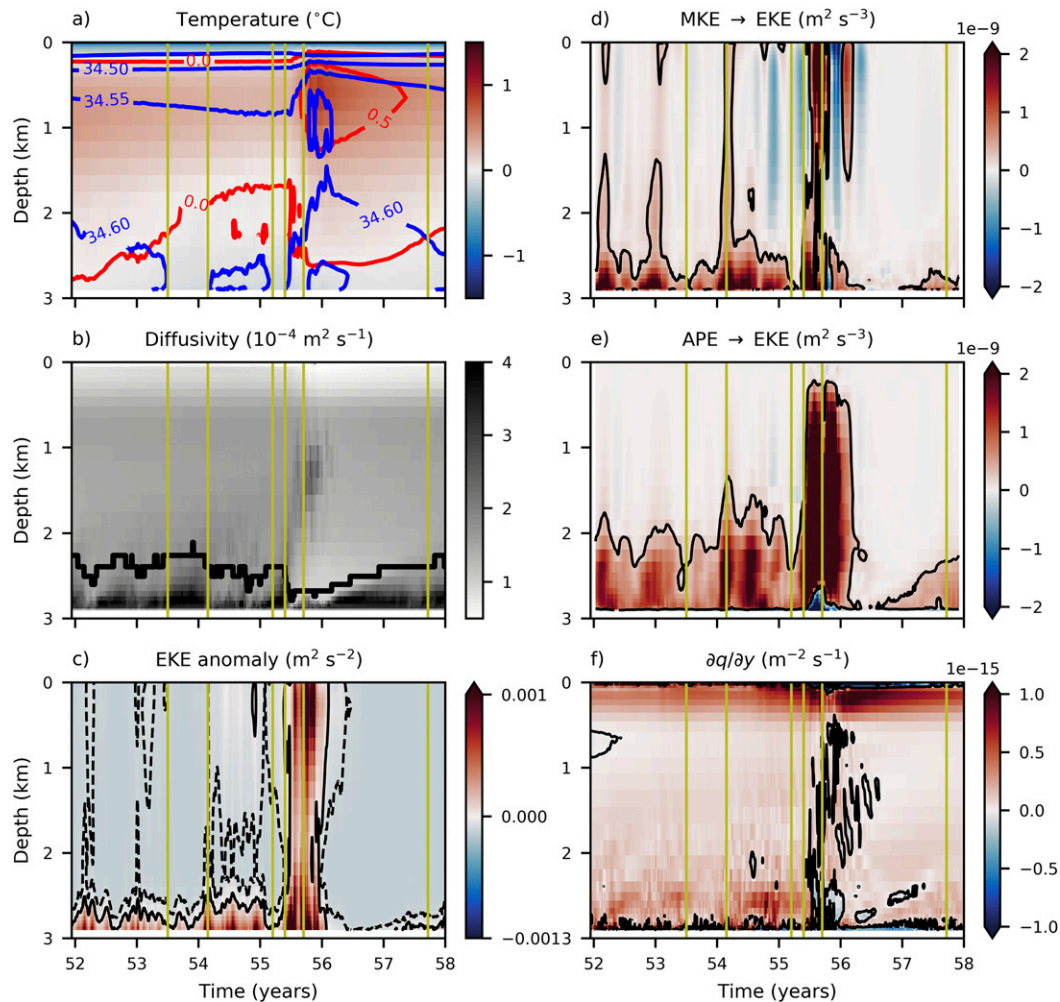


FIG. 4. Hovmöller diagrams at 340 km from the southern boundary (green line Figs. 3c,d). Shown are daily averages with the exception of (d) and (e), which are two months running means. (a) Temperature distribution with salinity (blue) and temperature (red) contours. (b) Vertical diffusivity with convection depth measured from the bottom (thick solid line). (c) EKE anomaly with the zero value contour (thin solid) and  $-10^{-4} \text{ m}^2 \text{ s}^{-2}$  contour (thin dashed). (d) Barotropic energy conversion from mean kinetic to eddy kinetic energy (positive) with  $0.25 \times 10^{-9} \text{ m}^2 \text{ s}^{-3}$  contour. (e) As in (d), but for baroclinic energy conversion from available potential to eddy kinetic energy (positive). (f) Meridional potential vorticity gradient with the zero contour in black. The yellow vertical lines indicate the time of the snapshots shown in Fig. 5.

depend on the chosen averaging time period. In this case, the net offshore heat transport is equivalent to a residual cooling of the continental slope area by  $0.04^\circ\text{C}$  in one year.

### c. Energetics of the instability events

The intrinsic variability can be understood in more detail from Figs. 4–6. To begin with, Fig. 4 shows Hovmöller diagrams (depth against time) at 340 km north of the southern boundary, because the variability is strongest in the offshore part of the ASF (Figs. 3b and 5). Shown is the last instability event of Fig. 3 (gray shaded area in Figs. 3a,b) with a daily resolution.

The energy conversion terms in Figs. 4d and 4e are based on a 2-month running mean.

During the buildup to the instability event from year 52 to the middle of year 55, the bottom water is overall cooling and freshening over time, as indicated by the  $0^\circ\text{C}$  temperature contour and the 34.6 salinity contour in Fig. 4a. The cooling and freshening signal originates from shelf water that is advected down the continental slope in the bottom Ekman layer (Figs. 2b,c). The flux of the relatively buoyant shelf water compared with the deep ocean leads to statically unstable conditions near the bottom and to enhanced vertical mixing and convection (Fig. 4b, shading). The resulting convection

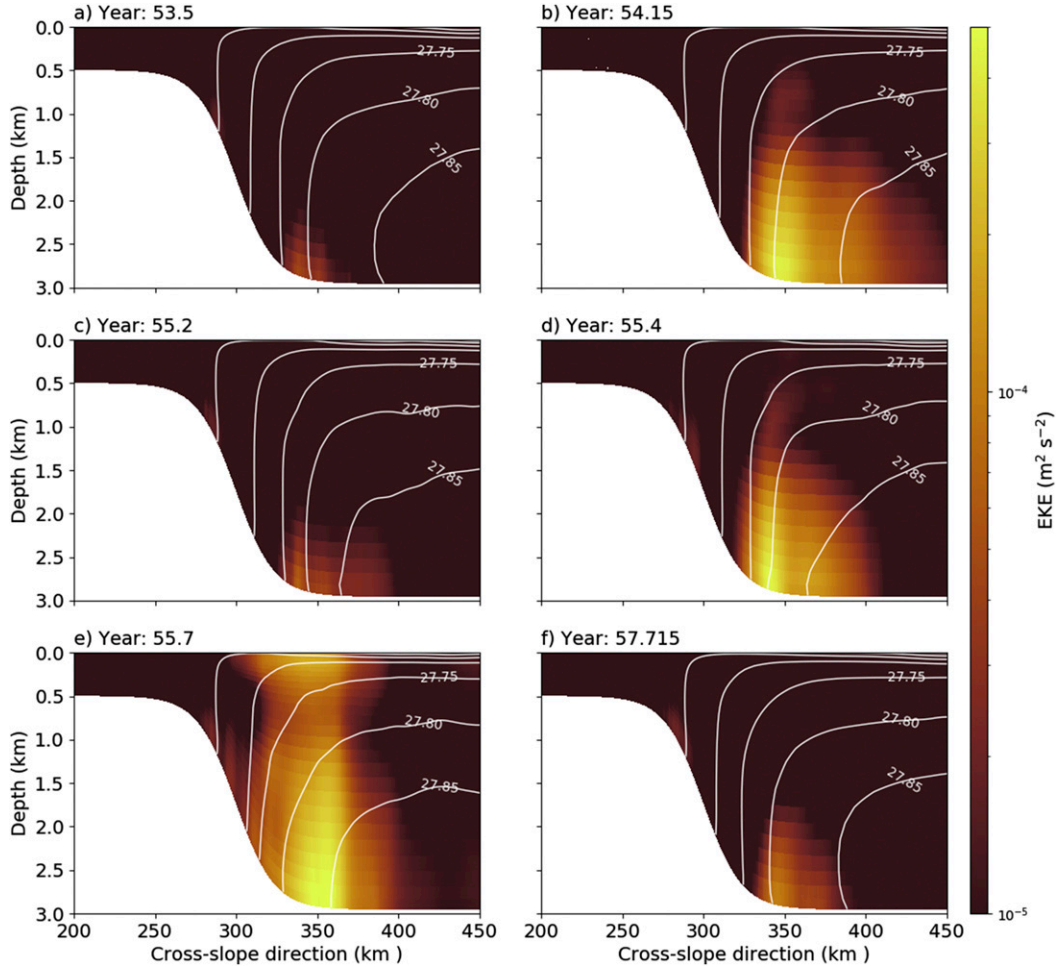


FIG. 5. Snapshots of EKE (shaded) and contours of potential density referenced to the surface ( $\text{kg m}^{-3}$ ). The time of the snapshots is indicated by the yellow vertical lines in Fig. 4.

depth, defined as the depth where the water parcels of the bottom grid cell reach their neutral buoyancy level when artificially lifted, is used here to approximate the depth of the bottom mixed layer and varies over time between 120 and 800 m (Fig. 4b, thick black contour). The supply of fresh continental shelf water deepens the bottom mixed layer, which is deepest just before an instability event. However, the deepening is not steadily toward the main instability event at the middle of year 55, but is disrupted by less intense instability events (an example of which is shown in Fig. 5b) which lead to a shallowing of the bottom mixed layer (Fig. 4b).

Figure 5 depicts snapshots in time of the cross-slope eddy kinetic energy (EKE) field to illustrate different stages of the intrinsic variability and to give further evidence that the instability events are triggered from the bottom. The EKE is the kinetic energy associated with the time varying flow, as indicated by the prime, and calculated as

$$\begin{aligned} \text{EKE} &= \frac{1}{2}(\langle u'^2 \rangle + \langle v'^2 \rangle) \\ &= \frac{1}{2}[(\langle u'^2 \rangle - \langle u \rangle^2) + (\langle v'^2 \rangle - \langle v \rangle^2)], \end{aligned} \quad (6)$$

using daily averaged model output of the horizontal velocity components  $\langle u \rangle$  and  $\langle v \rangle$ , and their squared values  $\langle u^2 \rangle$  and  $\langle v^2 \rangle$ . Maxima of EKE always exist near the sea floor at the lower continental slope (also see Fig. 4c). The elevated EKE is confined to the sea floor when the bottom mixed layer is deep (Figs. 5a,c,f), but extends further up in the water column during an instability event (Figs. 5b,d,e). Figure 5b is an example for a less intense instability event mentioned before, where the elevated EKE does not reach all the way to the surface unlike at year 55 (Fig. 5e). This latter “main” instability event first develops similarly (Fig. 5d), but the elevated EKE then reaches all the way to the surface, changing the stratification noticeably at the lower

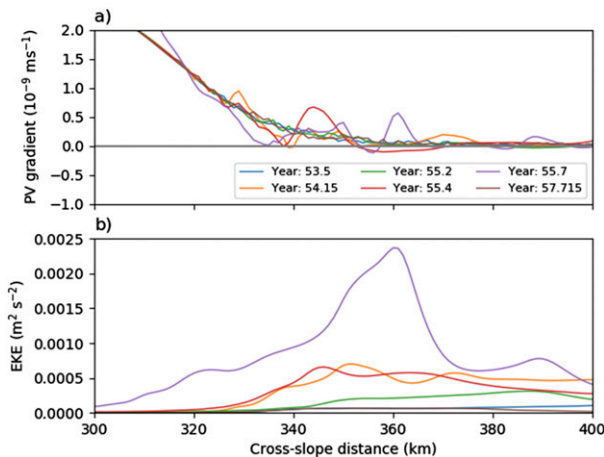


FIG. 6. (a) Depth-averaged barotropic potential vorticity gradient as a function of cross-slope distance. Zero crossings indicate barotropic unstable conditions. The topographic potential vorticity gradient is dominating at the continental slope (north of approximately 340 km from the southern boundary). (b) Depth-averaged EKE as a function of cross-slope distance.

continental slope and leading to a positive spike in the heat content as shown in Fig. 3a. The EKE declines again after the instability event (Fig. 5f).

EKE arises from conversion of energy from both mean kinetic energy (MKE) and available potential energy (APE). In the primitive equations, energy exchange from MKE to EKE is due to barotropic instability and energy exchange from APE to EKE is due to baroclinic instability. While the barotropic instability process is associated with the lateral shear and the baroclinic instability process with the vertical shear of a flow, they often occur concurrently. Such a mixed barotropic–baroclinic instability also exists here. Barotropic energy conversion, calculated as

$$\begin{aligned} \text{MKE} \rightarrow \text{EKE} &= -\langle u \rangle \frac{\partial}{\partial y} (\langle u'v' \rangle) \\ &= -\langle u \rangle \frac{\partial}{\partial y} (\langle uw \rangle - \langle u \rangle \langle v \rangle), \end{aligned} \quad (7)$$

is shown in Fig. 4d and baroclinic energy conversion, calculated as

$$\text{APE} \rightarrow \text{EKE} = \langle w'b' \rangle = \langle wb \rangle - \langle w \rangle \langle b \rangle \quad (8)$$

with the reduced gravity  $b = -g[(\rho - \rho_0)/\rho_0]$ , where  $\rho_0$  is the simulated mean density and  $w$  is the vertical velocity, is shown in Fig. 4e [for equations see Stewart and Thompson (2016) and Youngs et al. (2017), where only the advection of EKE due to the along-slope flow in cross-slope direction is of interest]. The range of values for barotropic and baroclinic energy conversion is similar, pointing toward a mixed barotropic–baroclinic

instability. Nevertheless, it is the baroclinic energy conversion which dominates the EKE production in the middle of the water column (Fig. 4e), whereas the barotropic energy conversion is rather confined to the bottom and surface (Fig. 4d). During an instability event, barotropic energy conversion dominates near the bottom which explains the existence of positive EKE anomalies during an instability event, even though EKE is also extracted and converted to APE. Accordingly, the along-slope current near the bottom is weaker during the event (not shown).

#### d. Barotropic and baroclinic instability criteria

Proxies for the jet's stability properties are used to analyze when conditions are favorable for barotropic or baroclinic instability. A necessary condition for barotropic instability is the zero-crossing of the PV gradient in the horizontal (here cross-slope direction). The quasigeostrophic PV gradient felt by the depth-averaged flow is calculated as

$$\beta^* = \beta + \frac{f_0}{H} \frac{\partial h_b}{\partial y} - \frac{\partial^2 \bar{u}^z}{\partial y^2}, \quad (9)$$

where the first term on the right hand side is the meridional gradient of the Coriolis parameter, the second term is the contribution from topography where  $h_b$  is the topographic height above  $H$ , and the last term represents the contribution from the meridional shear of the depth-averaged along-slope velocity.<sup>1</sup> A zero-crossing of the PV gradient therefore occurs when the shear at the flanks of the jet supersedes the stabilizing effects of Earth's rotation and topography. On the continental slope, the influence of the topography on the PV gradient dominates (Fig. 6a, left part of the panel) and limits the production of EKE (Fig. 6b and also Fig. 5). The influence of topography declines further north where the sea floor flattens. Barotropic unstable conditions become possible as indicated by the sign changes of the PV gradient. The position of the zero crossings correlate with the position of local maxima of the depth-averaged EKE, demonstrating the partly barotropic character of the instability events.

A necessary condition for baroclinic instability is met when the meridional gradient of PV changes sign

<sup>1</sup> Equation (9) can be derived by taking the derivative of the potential vorticity in cross-slope direction  $\partial q / \partial y = \beta^*$  with  $q = (f + \zeta)/h = (f_0 + \beta y + \zeta)/(H - h_b) \approx \beta y + (f_0/H)h_b - (\partial \bar{u}^z / \partial y)$ , where  $f = f_0 + \beta y$ ,  $h = H - h_b$ , and  $\zeta = -(\partial \bar{u}^z / \partial y)$  is the relative vorticity. To obtain the approximation  $q$  has been multiplied by  $(H + h_b)$  and only the large terms (using  $\beta y \ll f_0$  and  $h_b \ll H$ ) and terms that are relevant for the gradient calculation were kept.

in the vertical (e.g., Cushman-Roisin and Beckers 2011, chapter 17). Again, strictly speaking, the condition is only valid in the quasigeostrophic framework which, however, has been shown to apply beyond its formal limits (Williams et al. 2010). Here, PV is of the form

$$q = \frac{1}{\rho_0} [\hat{\mathbf{k}}(\langle \zeta \rangle + f) \cdot \nabla \rho], \quad (10)$$

where  $\hat{\mathbf{k}}$  is the vertical unit vector and  $\zeta$  is the relative vorticity. Figure 4f illustrates the meridional PV gradient in the water column at 340 km from the southern boundary as a function of time. Sign changes of the PV gradient are predominantly present near the sea floor and throughout the entire water column during the instability event, coinciding with the energy conversion from APE to EKE (Figs. 4e,f). Due to very similar timing of the onset of barotropic and baroclinic instabilities, it is not possible to distinguish which of the instabilities is the trigger of the events.

#### e. Sensitivity to surface momentum stress

The wind-driven overturning at the continental slope is a driver for the offshore directed bottom flux of relatively fresh shelf water, which eventually leads to the thick bottom mixed layer and instabilities of the ASF. The instability events can be expected to occur more often for stronger offshore bottom transport as it is equivalent to an acceleration of the bottom mixed layer formation process. To test this hypothesis, the sensitivity of the intrinsic ASF variability to the applied surface momentum stress is now briefly presented.

Figure 7 shows the HC time series for three simulations with varying surface momentum stress forcing equal to 50%, 100% (control run), and 150%. The experiments indeed reveal an increase in the time between two instability events for weaker momentum stress (10–15 years), and a shorter timing for stronger momentum stress (2–5 years). While the timing of the intermittent variability reveals a sensitivity to the surface momentum stress, the intensity of the instability events are of comparable magnitude.

## 4. Discussion

### a. Generation of a deep bottom mixed layer

The focus of this study is the ocean dynamics at the Antarctic continental slope. Under the conditions tested here, the continental shelf water is relatively buoyant as compared with the deep ocean. The wind-driven overturning circulation at the Antarctic margin, consisting of an onshore surface transport and a return flow in the bottom boundary layer (Figs. 2b,c), enables an export

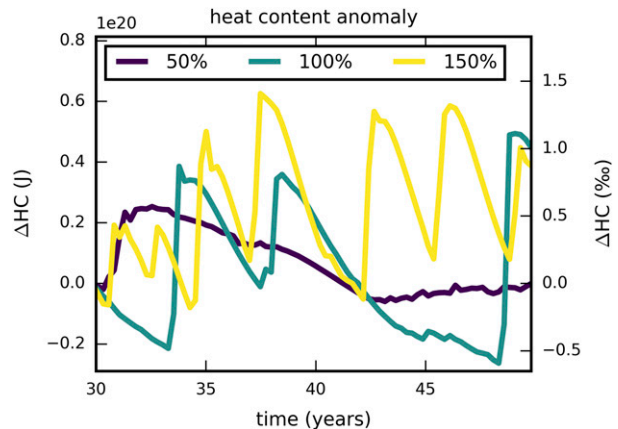


FIG. 7. Time series of ocean heat content anomaly for three simulations with varying surface momentum stress. The 100% simulation is the control run analyzed in the previous figures.

of the relatively fresh shelf water down the continental slope. The resulting freshwater flux leads to a deep bottom mixed layer at the lower slope in the presence of the ASF.

The bottom mixed layer thickness in the model is largest over the lower slope with maximum values up to 800 m. Physically, the thickening can be explained by enhanced vertical mixing resulting from static instabilities in the weakly stratified bottom layer. Artificial thickening, due to decreasing vertical grid resolution offshore using a terrain-following vertical coordinate system (for the bottom grid cell from 4 to 20 m, Fig. 1b), is small compared to the bottom mixed layer thickness of a few hundred meters. There are two aspects why the model might overestimate the bottom mixed layer thickness. First, the export of boundary layer water into the interior, which occurs largely along isopycnals, might be limited in the model due to the fact that the vertical grid and the isopycnals are nearly orthogonal in this region. Second, the model does not resolve the submesoscale which has been identified to sustain instabilities that promote a transport and ultimately increase the stratification, and with this reduce the bottom mixed layer thickness (Naveira Garabato et al. 2019).

Observations of bottom mixed layer depths along the Antarctic margin are rare, but there exists a glider dataset from north of the Antarctic Peninsula, where there is an eastward slope current, that captures the bottom mixed layer (Ruan et al. 2017). The measurements match the model results in that the bottom mixed layer is thickening toward the lower slope. The observed maximum bottom mixed layer thickness of 250 m is less than in the model. The comparison holds when using their definition for the bottom mixed layer of a  $\Delta 0.02 \text{ kg m}^{-3}$  density change, which results in an even deeper bottom mixed layer in the model (not shown).

However, measurements at the lower slope (deeper than 1000 m), where the process model showed the thickest mixed layer depth, do not exist.

Another observation of a deep bottom mixed layer along the Antarctic continental slope originates from the Weddell Sea (Fer et al. 2016). Yet, the identified generation process in that case is internal tides, which have been neglected in the present study for reasons of simplicity. Internal tides are likely to release their energy near critical slopes (where the topographic slope equals the slope of an internal wave ray) and for the  $M_2$  constituent near the critical latitude (where the wave frequency equals the local inertial frequency). In the Weddell Sea, such conditions occur simultaneously and form bottom mixed layers at the continental slope of 100-m depth.

### *b. Implications*

The formation of a deep bottom mixed layer has two implications for the type of ocean simulated in this study. First, the bottom mixed layer instabilities drive an intrinsic variability of the ASF that consists of short energetic events during which the water column becomes more stratified. The relaxation of the cross-slope density gradient goes along with a poleward transport of the relatively warm subsurface CDW. Stern et al. (2015) also investigate an aperiodic variability of an idealized slope jet in the high southern latitudes, but with an along-slope surface momentum stress in opposite direction to that of this study. Stern et al.'s (2015) results differ in that the jet becomes most unstable near the surface and subsequently drifts away in an offshore direction. Additionally, while the instability events are also of a mixed barotropic–baroclinic character, the onset of an instability event is connected to only baroclinic unstable conditions.

In this study, a threshold that might indicate the exact timing of an event was not found. However, the sensitivity analysis on the applied surface momentum stress revealed that the occurrence of the instability events responds to the strength of the wind-driven Ekman overturning. The result is in agreement with simulations performed by Nøst et al. (2011), which show larger overturning rates for a larger surface momentum stress (their Fig. 14). A relationship between the Ekman overturning and the position of the maximum along-slope surface momentum stress is not expected (Stewart and Thompson 2015). However, the buoyancy of the continental shelf water that is advected downslope should likewise have the potential to accelerate or decelerate the bottom mixed layer formation process (not tested, see also section 4c). If the observed freshening trend of continental shelf water (Schmidtke et al. 2014) continues, regions where DSW is formed today may

end up with weaker or no DSW formation in the future, and be vulnerable for the intermittent instabilities to develop.

Observational evidence of the intermittent variability on interannual to decadal time scales does not exist as continuously measured time series from, for example, moorings cover typically up to 3 years and are therefore too short. A CTD section from the Sabrina Coast at 120°E, East Antarctica, obtained during the BROKE campaign in austral summer 1996 though reveals a temperature snapshot [Fig. 5 from Bindoff et al. (2000) and Fig. 2 from Williams et al. (2011)] similar to the modeled temperature distribution during the instability event of Fig. 3d. Two existing measurements from the continental slope at a similar longitude from 2007 (Williams et al. 2011) and 2015 (Nitsche et al. 2017) confirm the existence of CDW near the bottom at different years. The two observations, however, do not represent a full transect across the slope. The closest full transect across the slope is at 118°E from 2015, but it only covers the upper 700 m. It is therefore questionable to imply constant hydrographic conditions from the existing observations. A transect further downstream at 110°E, which was also obtained during the BROKE campaign in 1996, indicates that this part of the Antarctic coastline is characterized by steeply downward sloping isopycnals in an onshore direction [Fig. 4 from Bindoff et al. (2000) and Fig. 2 from Williams et al. (2011)]. The hydrographic conditions thereby match the situation modeled in the present study between two instability events. A CTD section conducted in 2012 along 113°E confirms the strong temperature gradient across the shelf break with downward sloping isotherms at a different year (Peña-Molino et al. 2016).

Second, the findings contradict the hypothesis that all of the lower CDW is eventually converted into Antarctic Bottom Water (AABW) as part of the lower overturning cell (Marshall and Speer 2012). The strong vertical mixing in the boundary layer can lead to water mass transformation of the overlying water to a lighter density class. Observations from the Antarctic Peninsula show that such a water mass transformation is indeed active in the ocean (Ruan et al. 2017). The fact that the water mass can gain buoyancy away from the surface by enhanced bottom mixing suggests that significant amounts of deep water can be incorporated into CDW and be part of the Southern Ocean's upper overturning cell (Ruan et al. 2017).

### *c. Key parameters affecting the intrinsic variability*

There are many physical and numerical parameters affecting the dynamics of the ASF that have not been explored in this study. A brief discussion of selected parameters that are most relevant to the problem is

TABLE A1. Parameter choice for the process model of the Antarctic continental shelf break, part 1.

Parameter	Value	Description
$L_x$	400 km	Domain length
$L_y$	550 km	Domain width
$H$	3000 m	Maximum depth
$H_s$	500 m	Continental shelf depth
$L_{sl}$	150 km	Continental slope width
$L_{slc}$	300 km	Center continental slope
$L_{ic}$	100 km	Ice shelf draft width
$L_{icf}$	5 km	Ice shelf front width
$H_{ic}$	480 m	Maximum depth ice shelf draft
$H_{icf}$	200 m	Depth ice shelf front
$L_{\tau,x}$	200 km	Linear decrease of zonal momentum stress
$L_{\tau,y}$	200 km	Zero meridional momentum stress
$f_0$	$-1.31 \times 10^{-4} \text{ s}^{-1}$	Coriolis parameter, $f$ -plane constant
$\beta$	$8.89 \times 10^{-12} \text{ s}^{-1} \text{ m}^{-1}$	Coriolis parameter, beta-plane constant
$\Delta_t$	120 s/30 s	Baroclinic/barotropic time step
$\Delta_h$	1 km	Horizontal grid spacing
$N$	30	Number of vertical layers
$V_{\text{transform}}$	2	Transformation equation (vertical $S$ coordinate)
$V_{\text{stretching}}$	1	Stretching function
$\theta_{s,b}$	4/1	Surface/bottom stretching parameter
$T_{\text{cline}}$	20 m	Minimum water column thickness

presented now. First, the surface buoyancy forcing is important in setting the conditions for the continental shelf water that is critical for the development of a deep bottom mixed layer at the lower continental slope. The process model of the Antarctic continental shelf break developed here is similar to the model setup by [Stewart and Thompson \(2015\)](#), but their model differs in that strong DSW production is prescribed on the continental shelf. In their case, near-bottom isopycnals shoal to the south due to the export of DSW down the continental slope, and strong bottom mixed layer instabilities are inhibited. Their finding is in agreement with baroclinic instability theory that predicts stable conditions (suppression of baroclinic instability) if isopycnals are parallel to the bottom slope (e.g., [Isachsen 2011](#); [Pennel et al. 2012](#); [Stewart and Thompson 2013, 2016](#)). However, for a case of weak DSW production, [Stewart and Thompson \(2015\)](#) observe an intrinsic variability of the ASF similar to the present study (A. Stewart 2017, personal communication), supporting its physical robustness under the given boundary conditions.

Second, the slope of the continental shelf is critical for the topographic PV gradient that stabilizes the

TABLE A2. Parameter choice for the process model of the Antarctic continental shelf break, part 2.

Parameter	Value	Description
$\rho_0$	$1027 \text{ kg m}^3$	Reference density for Boussinesq approximation
$\tau_{\text{zon}}$	$-0.05 \text{ m}^2 \text{ s}^{-2}$	Zonal surface momentum stress minimum
$\tau_{\text{mer}}$	$0.025 \text{ m}^2 \text{ s}^{-2}$	Meridional surface momentum stress maximum
$T_{\text{sf}}$	$-1.85^\circ\text{C}$	Surface relaxation temperature
$T_{\text{br}}$	$-1.8^\circ\text{C}$	Maximum surface temperature to allow salt flux
$S_{\text{sf}}$	34.45	Surface relaxation salinity
$t_{\text{sf}}$	60 days	Relaxation time scale surface tracer flux
$t_{\text{nb}}$	1 day	Relaxation time scale northern boundary
$\text{tnu}_2$	$3 \text{ m}^2 \text{ s}^{-1}$	Horizontal harmonic mixing coefficient for tracer
$\text{visc}_2$	$40 \text{ m}^2 \text{ s}^{-1}$	Horizontal harmonic mixing coefficient for momentum
$\text{Akt}_{\text{bak}}$	$5 \times 10^{-5} \text{ m}^2 \text{ s}^{-1}$	Background vertical mixing coefficient for tracer
$\text{Akv}_{\text{bak}}$	$10^{-3} \text{ m}^2 \text{ s}^{-1}$	Background vertical mixing coefficient for momentum
$R_2$	$3 \times 10^{-3}$	Quadratic bottom drag coefficient

along-slope flow ([Fig. 6a](#); [Isachsen 2011](#)). The continental slope of the present domain is steep and therefore also able to maintain very steep isopycnals until baroclinic unstable conditions are met, manifested by the instability events. Less steep topographic slopes may allow instabilities to develop for less steep isopycnal slopes as well as closer to the continental shelf break, potentially leading to a larger onshore transport of CDW.

Third, the intensity of the instability events varies according to the amount of energy that is resolved with the model grid. The intrinsic variability is found for all tested horizontal resolutions, but the change in along-slope velocity during an instability event decreases for a horizontal resolution of less than 3 km to approximately 50% (not shown).

Finally, energy is extracted from the system at the bottom, in the model facilitated by the applied quadratic bottom stress. Using a coarser horizontal grid resolution of 3 km, sensitivity tests of the quadratic bottom drag [ $3 \times 10^{-4}$ ,  $1.5 \times 10^{-3}$ ,  $3 \times 10^{-3}$  (control run),  $6 \times 10^{-3}$ , and  $3 \times 10^{-2}$ ] have been conducted to support this discussion on the effect of the bottom drag on the intrinsic variability of the ASF. For smaller bottom drags less energy is dissipated and the ASC consequently speeds up. The instability events are more intense and there is a tendency toward a longer period of time between two events. To analyze the effect of the presence of submarine troughs on the development

TABLE A3. Overview of the used standard ROMS CPP options.

Option	Description
UV_ADV	Advection terms in momentum equations
UV_COR	Coriolis term in momentum equations
UV_VIS2	Harmonic horizontal mixing in momentum equations
SPLINES_VVISC	Splines reconstruction of vertical mixing
UV_QGRAD	Quadratic bottom friction in momentum equations
TS_C4HADVECTION	Fourth-order centered horizontal advection
TS_C4VADVECTION	Fourth-order centered vertical advection
TS_DIF2	Harmonic horizontal mixing
SALINITY	Salinity
SPLINES_VDIFF	Splines reconstruction of vertical diffusion
DJ_GRADPS	Splines density Jacobian ( <a href="#">Shchepetkin and McWilliams 2000</a> )
SOLVE3D	Solving 3D primitive equations
NONLIN_EOS	Nonlinear equation of state
AVERAGES	Writing out time-averaged data
MIX_GEO_UV	Horizontal mixing of momentum on geopotential (constant $z$ )
MIX_GEO_TS	Horizontal mixing of tracer on geopotential (constant $z$ )
LMD_MIXING	<a href="#">Large et al. (1994)</a> interior closure
LMD_CONVEC	Convection mixing due to shear instability
LMD_DDMIX	Double-diffusive mixing
LMD_RMIX	Diffusivity due to shear instability
LMD_SKPP	Surface boundary layer KPP mixing
ANA_GRID	Analytical model grid setup
ANA_INITIAL	Analytical initial conditions
ANA_SMFLUX	Analytical surface momentum stress
ANA_TOBC	Analytical tracers boundary conditions

of the intrinsic variability was out of scope for this discussion. Numerical simulations by [St-Laurent et al. \(2013\)](#), however, suggest that troughs introduce a three-dimensional circulation pattern that breaks up the zonally symmetric configuration of the present domain. It would be interesting to test in future work the effect of a trough on the generation of a deep bottom mixed layer.

## 5. Conclusions

This study focused on the dynamics of the ASF in an ocean process model for Antarctic continental shelves. Using instability theory, this study introduced a mixed barotropic–baroclinic instability of the ASF. A deep bottom mixed layer develops at the lower continental slope near the transition from sloping to flat bathymetry as a result of offshore bottom Ekman transport of relatively fresh continental shelf waters. The bottom mixed layer instabilities drive an intrinsic variability of the ASF. During instability events that last for approximately half

TABLE A4. Overview of the used CPP options unique to the ice-shelf/ocean ROMS version.

Option	Description
ICESHELF	Include ice shelf cavities
ICESHELF_3EQN_VBC	Three-equation ice/ocean thermodynamics
ANA_SEAICE	Simple open ocean sea ice model
SEAICE_WINTER	Prescribe constant winter surface fluxes

a year, the stratification increases, which weakens the ASF and the associated barrier between the cold continental shelf and the warmer CDW offshore.

The deep bottom mixed layer is a region of EKE production. High eddy activity and related onshore heat transport has so far only been connected to regions with elongated bathymetric features ([St-Laurent et al. 2013](#); [Daae et al. 2017](#)) or where the export of dense bottom water drives an interior return flow (e.g., [Thompson et al. 2014](#); [Stewart and Thompson 2015](#)). The mechanism discussed in this study, however, could be active in vast areas of the continental shelf around Antarctica where neither of the other two dominate.

To conclude, the intrinsic variability is a robust feature in the simulations, but warrants further investigation regarding the degree to which the mechanism changes in a submesoscale regime or is captured in realistic models, and regarding to how it translates to the ocean. Observations from the entire continental slope from shelf break to deep ocean would be valuable in order to confirm the maintenance of very steep isopycnals at the slope over several years.

*Acknowledgments.* The authors thank Andrew L. Stewart for useful discussions which helped to improve this work. The insightful comments by Pål Erik Isachsen and an anonymous reviewer were very much appreciated. WH is supported under the Australian Research Council Special Research Initiative Antarctic Gateway Partnership (SR140300001). The study contributed to the Australian Antarctic Division project 4287. The simulations presented here were conducted using resources from the National Computational Infrastructure (NCI), which is supported by the Australian Government.

## APPENDIX A

### Process Model Parameter Choices

The parameter choices for the process model of the Antarctic continental shelf break are given in

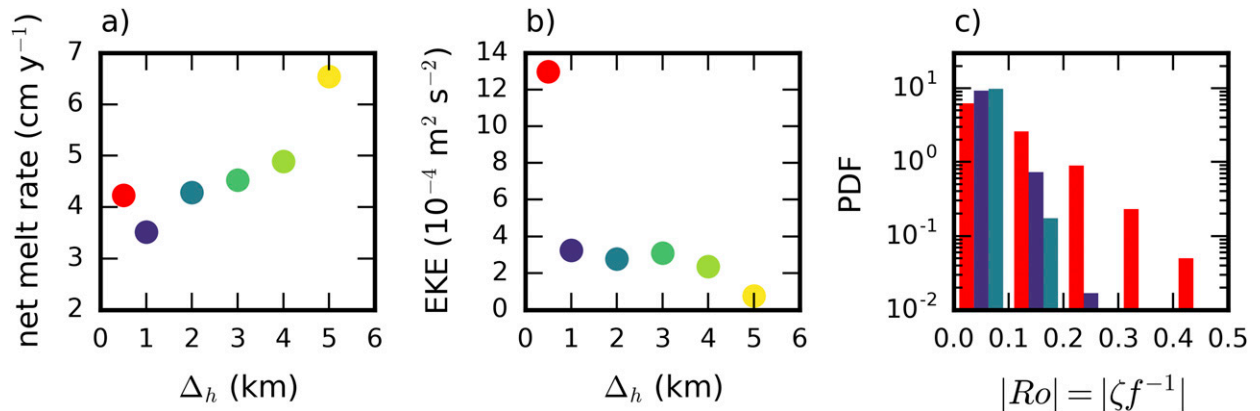


FIG. B1. Comparison of different horizontal grid resolutions  $\Delta_h$ , each given a separate color. (a) Net melt rate (excluding melting at the ice shelf front), (b) mean EKE on the continental slope (between the blue and green line in Figs. 3c,d), and (c) normalized histogram of Rossby number (Ro) at the third layer from the bottom on the continental slope for the three highest grid resolutions.

Tables A1 and A2. The forcing and domain specific parameters are prescribed analytically. The Coriolis parameter that varies linearly on a  $\beta$ -plane is calculated as

$$f = f_0 + \beta[y(j) - 550\,000],$$

with

$$f_0 = -1.31 \times 10^{-4} \text{ s}^{-1}, \quad \beta = 8.89 \times 10^{-12} \text{ m}^{-1} \text{ s}^{-1}, \\ y(0) = 0 \text{ m}.$$

The applied background vertical mixing coefficient for momentum is with  $10^{-3} \text{ m}^2 \text{ s}^{-1}$  relatively large. A simulation with a smaller background value ( $10^{-5} \text{ m}^2 \text{ s}^{-1}$ ) performed on a coarser grid resolution of 3 km revealed no changes in the occurrence or duration of the discussed intrinsic variability.

Tables A3 and A4 list all options that were used to perform the simulation, including the advection and mixing scheme. The ice-shelf/ocean specific options of Table A4 are not part of the standard ROMS distribution. Please contact the corresponding author regarding code accessibility.

## APPENDIX B

### Grid Resolution Analysis

This study uses a horizontal resolution of 1 km and 30 vertical layers. To resolve the mesoscale in the study area poses a challenge not only to global circulation models, but also regional models because of the small Rossby deformation radius at high latitudes. Previous studies suggested that a horizontal resolution on the order of 1 km is required (Nøst et al. 2011; Dinniman et al. 2012; St-Laurent et al. 2013; Hattermann et al.

2014; Stewart and Thompson 2015). To test the resolution dependency in our idealized setup we use a 20-yr mean (10-yr mean for the 500-m run) of the net melt rate and EKE as control variables (Fig. B1). Six simulations were run with grid resolutions of 0.5, 1, 2, 3, 4, and 5 km, the coarsest being comparable to what is considered to be a relatively high resolution global model ( $1/10^\circ$ ).

The net melt rate converges at 1-km horizontal resolution (Fig. B1a). Note that the net melt rate for all simulations is very small, because of cold ice shelf cavity temperatures. The lack of lateral boundaries in the model (Figs. 3c,d) change the cavity circulation which reduces the exchange with the continental shelf and keeps the cavity water cold. The EKE converges toward 1 km and then jumps toward a value about twice as large for 500-m horizontal resolution (Fig. B1b). This simulation starts to resolve submesoscale turbulence as seen from a sudden increase in the Rossby number  $Ro = \zeta/f$ , where  $\zeta = (\partial u/\partial y) - (\partial v/\partial x)$  is the vertical component of the relative vorticity (Fig. B1c).

A limited number of test simulations with double vertical resolution for 1- and 2-km horizontal resolution show a similar behavior to the 500-m run (not shown). However, doubling the vertical resolution leads to large pressure gradient errors, especially at the ice shelf front, which is why they are not used for the analysis. Pressure gradient errors at steep bathymetry are a known issue for models with terrain-following vertical coordinate systems (Haney 1991). Even for the vertical grid with 30 layers, the spurious velocities that occur at the ice shelf front are  $8.5 \text{ cm s}^{-1}$ . Along the continental slope which is the primary region of interest in this study, however, they reduce to reasonable values of less than  $0.2 \text{ cm s}^{-1}$  (0.7% of modeled ASC).

## APPENDIX C

## Surface Restoring

We restore the ocean surface and use an analytical expression to calculate the surface tracer flux  $F_{sf}$ . For a surface grid cell with height  $H_z$ , the tracer flux is given by the difference between the prescribed tracer value  $T_{sf}$  and the tracer value  $T$  prior to the relaxation, relative to a relaxation time scale  $t_{sf}$ :

$$F_{sf} = H_z \frac{1}{t_{sf}} (T_{sf} - T).$$

The chosen relaxation values for temperature and salinity match the density at 500-m depth of the northern boundary profile. This introduces convection to roughly that depth in the southern part of the domain where the influence of the northern boundary decreases. Note a constraint that is added for the salt flux. Only if surface temperatures prior to relaxation are close to surface freezing point (colder than  $T_{br} = -1.8^\circ\text{C}$ ), the salt flux will be nonzero. The resulting salt flux on the continental shelf is on average  $7 \times 10^{-8} \text{ psu ms}^{-1}$ . This indirectly implies the effect of brine rejection during sea ice formation.  $T_{br}$  is warmer than the surface freezing point temperature to increase the temperature range that permits a salt flux that represents sea ice growth.

## APPENDIX D

## List of Acronyms

AABW	Antarctic Bottom Water
ACC	Antarctic Circumpolar Current
APE	Available potential Energy
ASC	Antarctic Slope Current
ASF	Antarctic Slope Front
CDW	Circumpolar Deep Water
DSW	Dense shelf water
EKE	Eddy kinetic energy
MKE	Mean kinetic energy
PV	Potential vorticity
ROMS	Regional Ocean Modeling System

## REFERENCES

- Bindoff, N. L., M. A. Rosenberg, and M. J. Warner, 2000: On the circulation and water masses over the Antarctic continental slope and rise between  $80$  and  $150^\circ\text{E}$ . *Deep-Sea Res. II*, **47**, 2299–2326, [https://doi.org/10.1016/S0967-0645\(00\)00038-2](https://doi.org/10.1016/S0967-0645(00)00038-2).
- Cougnon, E. A., B. K. Galton-Fenzi, A. J. S. Meijers, and B. Legrésy, 2013: Modeling interannual dense shelf water export in the region of the Mertz Glacier Tongue (1992–2007). *J. Geophys. Res. Oceans*, **118**, 5858–5872, <https://doi.org/10.1002/2013JC008790>.
- Cushman-Roisin, B., and J.-M. Beckers, 2011: *Introduction to Geophysical Fluid Dynamics: Physical and Numerical Aspects*. International Geophysics, Vol. 1010, Academic Press, 789 pp.
- Daae, K., T. Hattermann, E. Darelus, and I. Fer, 2017: On the effect of topography and wind on warm water inflow - An idealized study of the southern Weddell Sea continental shelf system. *J. Geophys. Res. Oceans*, **122**, 2622–2641, <https://doi.org/10.1002/2016JC012541>.
- Depoorter, M. A., J. L. Bamber, J. A. Griggs, J. T. M. Lenaerts, S. R. M. Ligtenberg, M. R. van den Broeke, and G. Moholdt, 2013: Calving fluxes and basal melt rates of Antarctic ice shelves. *Nature*, **502**, 89–92, <https://doi.org/10.1038/nature12567>.
- Dinniman, M. S., J. M. Klinck, and W. O. Smith, 2011: A model study of Circumpolar Deep Water on the West Antarctic Peninsula and Ross Sea continental shelves. *Deep-Sea Res. II*, **58**, 1508–1523, <https://doi.org/10.1016/j.dsr2.2010.11.013>.
- , —, and E. E. Hofmann, 2012: Sensitivity of Circumpolar Deep Water transport and ice shelf basal melt along the West Antarctic Peninsula to changes in the winds. *J. Climate*, **25**, 4799–4816, <https://doi.org/10.1175/JCLI-D-11-00307.1>.
- , X. S. Asay-Davis, B. K. Galton-Fenzi, P. R. Holland, A. Jenkins, and R. Timmermann, 2016: Modeling ice shelf/ocean interaction in Antarctica: A review. *Oceanography*, **29**, 144–153, <https://doi.org/10.5670/oceanog.2016.106>.
- Fer, I., E. Darelus, and K. B. Daae, 2016: Observations of energetic turbulence on the Weddell Sea continental slope. *Geophys. Res. Lett.*, **43**, 760–766, <https://doi.org/10.1002/2015GL067349>.
- Galton-Fenzi, B. K., J. R. Hunter, R. Coleman, S. J. Marsland, and R. C. Warner, 2012: Modeling the basal melting and marine ice accretion of the Amery Ice Shelf. *J. Geophys. Res.*, **117**, C09031, <https://doi.org/10.1029/2012JC008214>.
- Gwyther, D. E., B. K. Galton-Fenzi, J. R. Hunter, and J. L. Roberts, 2014: Simulated melt rates for the Totten and Dalton ice shelves. *Ocean Sci.*, **10**, 267–279, <https://doi.org/10.5194/os-10-267-2014>.
- Haney, R. L., 1991: On the pressure gradient force over steep topography in sigma coordinate ocean models. *J. Phys. Oceanogr.*, **21**, 610–619, [https://doi.org/10.1175/1520-0485\(1991\)021<0610:OTPGFO>2.0.co;2](https://doi.org/10.1175/1520-0485(1991)021<0610:OTPGFO>2.0.co;2).
- Hattermann, T., L. H. Smedsrud, O. A. Nøst, J. M. Lilly, and B. K. Galton-Fenzi, 2014: Eddy-resolving simulations of the Fimbul Ice Shelf cavity circulation: Basal melting and exchange with open ocean. *Ocean Modell.*, **82**, 28–44, <https://doi.org/10.1016/j.ocemod.2014.07.004>.
- Isachsen, P. E., 2011: Baroclinic instability and eddy tracer transport across sloping bottom topography: How well does a modified Eady model do in primitive equation simulations? *Ocean Modell.*, **39**, 183–199, <https://doi.org/10.1016/j.ocemod.2010.09.007>.
- Jacobs, S. S., 1991: On the nature and significance of the Antarctic Slope Front. *Mar. Chem.*, **35**, 9–24, [https://doi.org/10.1016/S0304-4203\(09\)90005-6](https://doi.org/10.1016/S0304-4203(09)90005-6).
- Large, W. G., and S. G. Yeager, 2009: The global climatology of an interannually varying air-sea flux data set. *Climate Dyn.*, **33**, 341–364, <https://doi.org/10.1007/s00382-008-0441-3>.
- , J. C. McWilliams, and S. C. Doney, 1994: Oceanic vertical mixing: A review and a model with a nonlocal boundary-layer parameterization. *Rev. Geophys.*, **32**, 363–403, <https://doi.org/10.1029/94RG01872>.

- Marshall, J., and K. Speer, 2012: Closure of the meridional overturning circulation through Southern Ocean upwelling. *Nat. Geosci.*, **5**, 171–180, <https://doi.org/10.1038/ngeo1391>.
- Mathiot, P., H. Goosse, T. Fichefet, B. Barnier, and H. Gallée, 2011: Modelling the seasonal variability of the Antarctic Slope Current. *Ocean Sci.*, **7**, 455–470, <https://doi.org/10.5194/os-7-455-2011>.
- Moffat, C., B. Owens, and R. C. Beardsley, 2009: On the characteristics of Circumpolar Deep Water intrusions to the west Antarctic Peninsula continental shelf. *J. Geophys. Res.*, **114**, C05017, <https://doi.org/10.1029/2008JC004955>.
- Naveira Garabato, A. C., and Coauthors, 2019: Rapid mixing and exchange of deep-ocean waters in an abyssal boundary current. *Proc. Natl. Acad. Sci. USA*, **116**, 13 233–13 238, <https://doi.org/10.1073/pnas.1904087116>.
- Nitsche, F. O., D. Porter, G. Williams, E. A. Cougnon, A. D. Fraser, R. Correia, and R. Guerrero, 2017: Bathymetric control of warm ocean water access along the East Antarctic Margin. *Geophys. Res. Lett.*, **44**, 8936–8944, <https://doi.org/10.1002/2017GL074433>.
- Nøst, O. A., M. Biuw, V. Tverberg, C. Lydersen, T. Hattermann, Q. Zhou, L. H. Smedsrud, and K. M. Kovacs, 2011: Eddy overturning of the Antarctic Slope Front controls glacial melting in the Eastern Weddell Sea. *J. Geophys. Res.*, **116**, C11014, <https://doi.org/10.1029/2011JC006965>.
- Peña-Molino, B., M. S. McCartney, and S. R. Rintoul, 2016: Direct observations of the Antarctic Slope Current transport at 113E. *J. Geophys. Res. Oceans*, **121**, 7390–7407, <https://doi.org/10.1002/2015JC011594>.
- Pennel, R., A. Stegner, and K. Béranger, 2012: Shelf impact on buoyant coastal current instabilities. *J. Phys. Oceanogr.*, **42**, 39–61, <https://doi.org/10.1175/JPO-D-11-016.1>.
- Petty, A. A., D. L. Feltham, and P. R. Holland, 2013: Impact of atmospheric forcing on Antarctic continental shelf water masses. *J. Phys. Oceanogr.*, **43**, 920–940, <https://doi.org/10.1175/JPO-D-12-0172.1>.
- Pritchard, H. D., S. R. M. Ligtenberg, H. A. Fricker, D. G. Vaughan, M. R. van den Broeke, and L. Padman, 2012: Antarctic ice-sheet loss driven by basal melting of ice shelves. *Nature*, **484**, 502–505, <https://doi.org/10.1038/nature10968>.
- Rignot, E., S. Jacobs, J. Mouginot, and B. Scheuchl, 2013: Ice-shelf melting around Antarctica. *Science*, **341**, 266–270, <https://doi.org/10.1126/science.1235798>.
- Rintoul, S. R., A. Silvano, B. Pena-Molino, E. van Wijk, M. Rosenberg, J. S. Greenbaum, and D. D. Blankenship, 2016: Ocean heat drives rapid basal melt of the Totten Ice Shelf. *Sci. Adv.*, **2**, e1601610, <https://doi.org/10.1126/sciadv.1601610>.
- Ruan, X., A. F. Thompson, M. M. Flexas, and J. Sprintall, 2017: Contribution of topographically generated submesoscale turbulence to Southern Ocean overturning. *Nat. Geosci.*, **10**, 840–845, <https://doi.org/10.1038/ngeo3053>.
- Schmidtke, S., K. J. Heywood, A. F. Thompson, and S. Aoki, 2014: Multidecadal warming of Antarctic waters. *Science*, **346**, 1227–1231, <https://doi.org/10.1126/science.1256117>.
- Shchepetkin, A. F., and J. C. McWilliams, 2000: The regional ocean modeling system: A split-explicit, free surface, topography-following coordinate model. Geophysics and Planetary Physics, University of California, Los Angeles, 31 pp.
- , and —, 2005: The Regional Oceanic Modeling System (ROMS): A split-explicit, free-surface, topography-following-coordinate oceanic model. *Ocean Modell.*, **9**, 347–404, <https://doi.org/10.1016/j.ocemod.2004.08.002>.
- Silvano, A., S. R. Rintoul, and L. Herraiz-Borreguero, 2016: Ocean-ice shelf interaction in East Antarctica. *Oceanography*, **29**, 130–143, <https://doi.org/10.5670/oceanog.2016.105>.
- St-Laurent, P., J. M. Klinck, and M. S. Dinniman, 2013: On the role of coastal troughs in the circulation of warm Circumpolar Deep Water on Antarctic shelves. *J. Phys. Oceanogr.*, **43**, 51–64, <https://doi.org/10.1175/JPO-D-11-0237.1>.
- Stern, A., L.-P. Nadeau, and D. Holland, 2015: Instability and mixing of zonal jets along an idealized continental shelf break. *J. Phys. Oceanogr.*, **45**, 2315–2338, <https://doi.org/10.1175/JPO-D-14-0213.1>.
- Stewart, A. L., and A. F. Thompson, 2013: Connecting Antarctic cross-slope exchange with Southern Ocean overturning. *J. Phys. Oceanogr.*, **43**, 1453–1471, <https://doi.org/10.1175/JPO-D-12-0205.1>.
- , and —, 2015: Eddy-mediated transport of warm Circumpolar Deep Water across the Antarctic shelf break. *Geophys. Res. Lett.*, **42**, 432–440, <https://doi.org/10.1002/2014GL062281>.
- , and —, 2016: Eddy generation and jet formation via dense water outflows across the Antarctic continental slope. *J. Phys. Oceanogr.*, **46**, 3729–3750, <https://doi.org/10.1175/JPO-D-16-0145.1>.
- Thompson, A. F., K. J. Heywood, S. Schmidtke, and A. L. Stewart, 2014: Eddy transport as a key component of the Antarctic overturning circulation. *Nat. Geosci.*, **7**, 879–884, <https://doi.org/10.1038/ngeo2289>.
- , A. L. Stewart, P. Spence, and K. J. Heywood, 2018: The Antarctic Slope Current in a changing climate. *Rev. Geophys.*, **56**, 741–770, <https://doi.org/10.1029/2018RG000624>.
- Whitworth, T., A. H. Orsi, S. J. Kim, W. D. Nowlin, and R. A. Locarnini, 1998: Water masses and mixing near the Antarctic Slope Front. *Ocean, Ice and Atmosphere: Interactions at the Antarctic Continental Margin*, Antarctic Research Series, Vol. 75, Amer. Geophys. Union, 1–27, <https://doi.org/10.1029/AR075p0001>.
- Williams, P. D., P. L. Read, and T. W. Haine, 2010: Testing the limits of quasi-geostrophic theory: Application to observed laboratory flows outside the quasi-geostrophic regime. *J. Fluid Mech.*, **649**, 187–203, <https://doi.org/10.1017/S0022112009993405>.
- Williams, G. D., A. J. S. Meijers, A. Poole, P. Mathiot, T. Tamura, and A. Klocker, 2011: Late winter oceanography off the Sabrina and BANZARE coast (117–128°E), East Antarctica. *Deep-Sea Res. II*, **58**, 1194–1210, <https://doi.org/10.1016/j.dsr2.2010.10.035>.
- Youngs, M. K., A. F. Thompson, A. Lazar, and K. J. Richards, 2017: ACC meanders, energy transfer, and mixed barotropic-baroclinic instability. *J. Phys. Oceanogr.*, **47**, 1291–1305, <https://doi.org/10.1175/JPO-D-16-0160.1>.